Surface Softening in Metal–Ceramic Sliding Contacts: An Experimental and Numerical Investigation

Pantcho Stoyanov,*,†,‡,# Rolf Merz,§ Pedro A. Romero,† Felix C. Wählisch,∥ Oscar Torrents Abad,∥ Robert Gralla,∥ Priska Stemmer,⊥ Michael Kopnarski,§ Michael Moseler,† Roland Bennewitz,∥ and Martin Dienwiebel†,‡

†Fraunhofer-Institute for Mechanics of Materials IWM-MicroTribology Center μTC, Wöhlerstrasse 11, 79108 Freiburg, Germany, ‡Karlsruhe Institute of Technology KIT, Institute for Applied Materials IAM, Kaiserstrasse 12, 76131 Karlsruhe, Germany, §IFOS-Institute für Oberflächen- und Schichtanalytik GmbH, Trippstadter Strasse 120, 67663 Kaiserslautern, Germany, ∥INM — Leibniz Institute for New Materials and Physics Department, Saarland University, Campus D2 2,66123 Saarbrücken, Germany, and ⊥Institute of Product Engineering, University Duisburg-Essen, Lotharstrasse 1, 47057 Duisburg, Germany #Present address: Innovation Ventures Group, Kennametal Inc., 1600 Technology Way, Latrobe, PA 15650, USA.

ABSTRACT This study investigates the tribolayer properties at the interface of ceramic/metal (*i.e.*, WC/W) sliding contacts using various experimental approaches and classical atomistic simulations. Experimentally, nanoindentation and micropillar compression tests, as well as adhesion mapping by means of atomic force microscopy, are used to evaluate the strength of tungsten–carbon tribolayers. To capture the influence of environmental conditions, a detailed chemical and structural analysis is performed on the worn surfaces by means of XPS mapping and depth profiling along with transmission electron microscopy of the debris particles. Experimentally, the results indicate a decrease in hardness and modulus of the worn surface compared to the unworn one. Atomistic simulations of nanoindentation on deformed and undeformed specimens are used to probe the strength of the WC tribolayer and despite the fact that the simulations do not include oxygen, the simulations correlate well with the experiments on deformed and undeformed surfaces, where the difference in behavior is attributed to the bonding and structural differences of amorphous and crystalline W–C. Adhesion mapping indicates a decrease in surface adhesion, which based on chemical analysis is attributed to surface passivation.

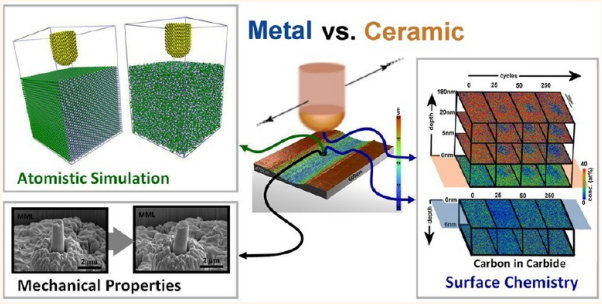

KEYWORDS: nanomechanics · adhesion · third-body · xps · molecular dynamics · tungsten · tungsten carbide

The advancement of high-performance energy generation technologies depends heavily on the development of materials, which can withstand extreme environmental and contact conditions (*i.e.*, high contact pressures, radiation, large temperature ranges, and corrosive environments, all of which can degrade the physical properties). In the field of aerospace engineering, the conditions in which materials are expected to operate are becoming increasingly more demanding. Due to the large number of complex contacting and moving mechanical-assemblies in such applications, the lifetime of structures is limited by the mechanical and tribological (*i.e.*, friction and wear) properties of the employed materials. Degradation of these physical properties will lead to failure of the moving components and subsequently to severe damage of the machinery.

The sliding of components is known to result in third body formation, which characteristically consists of mechanical mixing and grain refinement in the near surface region[1,2] as well as transfer film formation on the counterface.[1,3,4] Understanding the behavior of these so-called third bodies can help to optimize the tribological response of sliding components by selecting the right combination of materials, environmental and contact conditions (*e.g.*, pressure, contact area)[5] leading to new engineering solutions that can operate in more demanding applications. Numerous studies have used various *in situ* and *ex situ* approaches to better understand the evolution of interfacial processes[6–8] and to correlate them to the friction and wear behavior.

In our recent studies, we have studied the nanoscale sliding friction phenomena of

* Address correspondence to pantcho.stoyanov@mail.mcgill.ca.

Received for review October 19, 2014 and accepted December 21, 2014.

Published online December 21, 2014
10.1021/nn505968m

materials for extreme conditions (*i.e.*, W, W:C, DLC) by linking *in situ* experiments with atomistic simulations.[9−11] The experimental approach in our studies identified the main velocity accommodation modes and the molecular dynamic simulations captured the nanoscale mechanisms at the sliding interfaces leading to the observed friction and wear behavior. In our first study, we found that the sliding of tungsten against tungsten-carbide results in plastic deformation of the tungsten surface, leading to grain refinement, and the formation of a mechanically mixed amorphous layer on the WC counter body.[9] In our subsequent study, we compared this behavior to lubricated metal/ceramic systems (*i.e.*, hexadecane as a lubricant), which showed a less pronounced third-body formation due to much lower dissipated frictional power.[10] For the case of a-C:H against W,[11] the dry sliding condition results in higher frictional resistance and significantly more material transfer compared with lubricated conditions. While a great amount of information has been generated on the third body formation process and velocity accommodation modes in sliding contacts using these methodologies, there still remains an uncertainty about the evolution of the strength (*e.g.*, hardness and reduced modulus) and of adhesion and cohesion of these tribofilms as well as how these properties influence the friction and wear of the sliding system.

Several studies have been performed using microindentaion techniques in order to address these questions.[4,12−15] For instance, Wang *et al.*[4] used microindentaion to study the mechanically deformed surfaces of Pb−Sn in various environments. The authors observed softening of the near surface region in vacuum. However, the hardness of the worn surface in air showed a slight increase, which was attributed to the formation of tin oxides. Rupert *et al.*[14] evaluated hardness of the worn near-surface microstructure in nanocrystalline Ni−W and found an apparent deviation from Archard's law for the finest grain size structures. While these two studies have provided valuable insights on the microhardness of tribofilms, it is important to investigate how these properties translate to smaller scale mechanically mixed layers and transfer films given the relatively large contact area in microindentation and how they translate to third bodies of different structures (*e.g.*, amorphous tribofilms).

In a recent study, Battaile *et al.*[13] investigated the hardness and strength of tribofilms created by a sliding process on single crystal nickel. The authors provided a direct comparison between nanoindentaion and micropillar compression techniques. Interestingly, the two mechanical testing methods revealed an apparent contradiction on the strength of the tribofilm; while the nanoindentation results suggested that the tribofilm is stronger, the microcompression tests indicated that the wear track is nearly twice as soft compared to the unworn surface. This contradiction was explained by the fact that defects (*i.e.*, generated by the wear) decrease the strength of pillars whereas nanoindentations showed higher hardness values for the worn surface compared to the unworn due to the fine-grained structure. Thus, the authors in this study recommended that interpretation of the experiments should be performed with great caution. Yet, the question of whether these so-called third bodies are harder or softer than the unworn materials remains unanswered.

Our aim here is to resolve some of these confusions and provide a better understanding of the nanoscale phenomena in metal/ceramic sliding couples by studying the deformation mechanisms and nanomechanical properties of the third bodies using an experimental and numerical atomistic approach. Understanding the behavior and properties of these nanoscale interfacial processes will support the design of low friction and high wear resistant materials, which will help overcome many of the challenges in high-performance sliding components. This study is unique in that certain aspects of the deformation mechanisms underlying the experimentally observed results are further investigated using molecular dynamics indentations. We chose tungsten-based materials for their high mechanical stability in extreme contact and environmental conditions. Experimentally, nanoindentation and micropillar compression are used to investigate the hardness and reduced modulus of tribofilms generated in WC/W tribocouples, while atomic force microscopy is used for measuring the surface adhesion. Molecular dynamics simulations of nanoindentation are performed on mechanically mixed tribolayers to elucidate the nanoscale processes leading to the experimentally observed mechanical properties. To capture the influence of environmental conditions, a detailed chemical and structural analysis is performed on the worn surfaces by means of XPS mapping and depth profiling as well as transmission electron microscopy (TEM) of the debris particles.

RESULTS

In this study, third bodies are created in WC/W tribocouples at various cycle numbers during the running-in and steady state stages. The friction response of this sliding system is typical for dry metallic sliding contacts and consistent with previously reported results on this tribosystem;[9,10] upon initial sliding, the coefficient of friction is approximately 0.2 and subsequently, the friction increases up to 0.6 where it remains nearly constant during steady state sliding. The wear response of this sliding system follows a slightly different trend, where the worn area of the tungsten specimen increases with the higher cycle number. Correspondingly, the variations in roughness revealed by topography measurements indicate an increase in the amount of mechanically mixed material with the increase in cycle number.

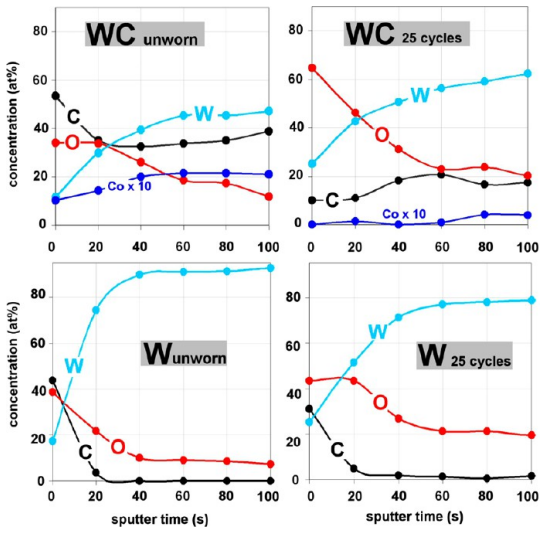

Figure 1. XPS sputter profiles (2 keV Ar^+) for a 5 nm depth (100s sputter time) of the tungsten carbide ball and tungsten platen in the unworn state and after 25 cycles. The analyzed spot size is about 110 μm, which is similar to the contact area. The cobalt concentration in the diagrams is multiplied by a factor 10.

Cross-sectional SEM analysis of the tungsten wear tracks are performed after the various cycle numbers during the running-in and the steady state stage (not shown here). The analysis shows a grain-refined layer in the near surface region caused by plastic deformation during sliding (*i.e.*, nucleation of dislocations and possibly rotation of clusters). In parallel, the tungsten carbide counter face forms a mechanically mixed amorphous layer within the contact area, as revealed by TEM images.[10] While the existence of these third bodies is already known, here the aim is to provide a better understanding of the chemical evolution leading to the variation in microstructure.

Chemical Characterization of WC/W Third Body. The surface chemistry of both counter faces (*i.e.*, tungsten and tungsten carbide) is analyzed by means of XPS spectroscopy in the unworn and worn state (*i.e.*, after 25 cycles). The results are plotted in Figure 1 as atomic concentration *vs* sputtering time. Initially, the unworn tungsten carbide sputter profiles show a carbon concentration of ~55 atom %, an oxygen concentration of about ~35 atom % and a tungsten concentration of about ~10 atom %. Cobalt, the binding component, is detected with approximately 1 atom %. After a 1 nm sputtering depth, the carbon and oxygen enrichment at the surface decreases and tungsten and carbon approach a stoichiometry of 1:1.

After 25 cycles of sliding, a significant change in the atomic composition of the tungsten carbide surface is observed; an enrichment of tungsten (>20 atom %), an enrichment of oxygen (>60 atom %), and a decrease of carbon concentrations (<10 atom %). In addition, nearly no cobalt is detected. This already indicates the formation of a thin layer on the tungsten carbide specimen during sliding, composed of tungsten oxides (W_2O_3, WO_2 or WO_3) as well as metallic tungsten.

The tungsten specimen shows a different behavior. In the unworn state, the initial carbon and oxygen concentrations (*i.e.*, without sputtering) are approximately 40 atom % with a tungsten concentration of 20 atom %. Subsequently, the oxygen concentration drops to ~8 atom % after sputtering about 2 nm, while the carbon concentration decreases drastically to nearly 0 atom % and remains absent for higher sputtering depths (>1 nm). This initial carbon composition is common for metallic surfaces handled under ambient environmental conditions, where a thin organic film is present on the surface due to environmental hydrocarbons. Such hydrocarbon layers are still present even after preanalysis cleaning in ultrasonic baths with different solvents (cyclohexane, isopropanol and acetone).

In the worn state, the oxygen concentration on the other hand, remains constant up to 1 nm and then decreases to 20 atom % at 3 nm. Correspondingly, the tungsten concentration increases at a high rate for the 2 nm after which it approaches 80 atom %. The oxygen to tungsten concentration ratio at a sputter depth of 5 nm indicates that metallic tungsten dominates the contact area, with at most 13 atom % of the tungsten being bound as WO_2.

The chemical nature of the remaining carbon within the material on the tungsten and tungsten carbide counter face is analyzed by XPS after 250 cycles, as presented by C 1s, O 1s and W 4f detail spectra in Figure 2. The majority of the carbon is bound in aliphatic hydrocarbons (C 1s binding energy E_B = 285 eV). Carbon bound in tungsten carbide (E_B = 283 eV) is only detected on the tungsten carbide counterface in the unworn and worn state (after 250 cycles). No tungsten carbide is detected on the tungsten specimen before and after sliding. Comparing the worn with the unworn state of the tungsten carbide ball, the W 4f doublet photoelectron lines show a small shift of 0.3 eV to lower binding energies, indicating transfer of metallic tungsten from the tungsten to the tungsten carbide ball. These observations are consistent with previous analysis of WC/W tribo couples by means of TEM.[10]

A lateral resolved 3D tomographical XPS chemical analysis within the contact area of the tungsten carbide and the tungsten specimen (Figures 3–5) is performed in order to provide a better understanding on the lateral distribution of the different binding states. Figures 3–5 show atomic concentration maps of oxygen bound as tungsten oxide, carbon bound as tungsten carbide, and tungsten bound as metallic tungsten, respectively. The highest oxide concentrations (40 atom %, red color), are observed in the contact area of the tungsten carbide ball, as well as in the center of the wear track of the tungsten platen as shown in Figure 3. In addition, the spot size of the contact area in the oxide maps increases with

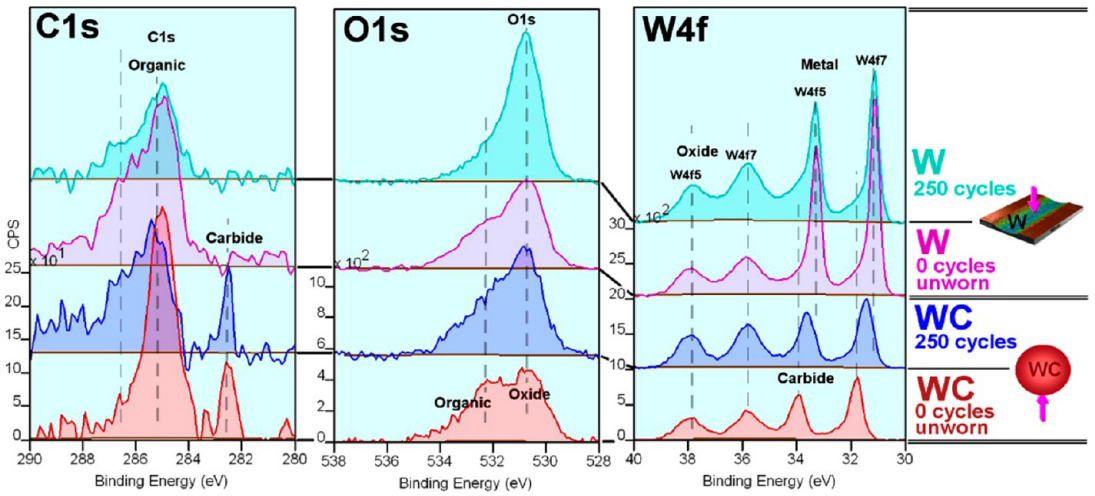

Figure 2. XPS detail spectra of C 1s, O 1s. and W 4f photoelectron lines for the tungsten carbide sphere and the tungsten plate in the unworn state and after 250 sliding cycles without sputtering. The different chemical states of carbon, oxygen and tungsten are distinguished according the chemical shift of the electron binding energy. The C 1s binding energy corresponds to organically bound carbon and carbon in carbide, the O 1s binding energy corresponds to organic and oxidic bound oxygen, and the binding energy of the W 4f7/2 to W 4f5/2 doublet corresponds to tungsten in metal, carbide and oxide (shown as vertical dashed lines). The analyzed spot size is about 110 μm, which is similar to the contact area.

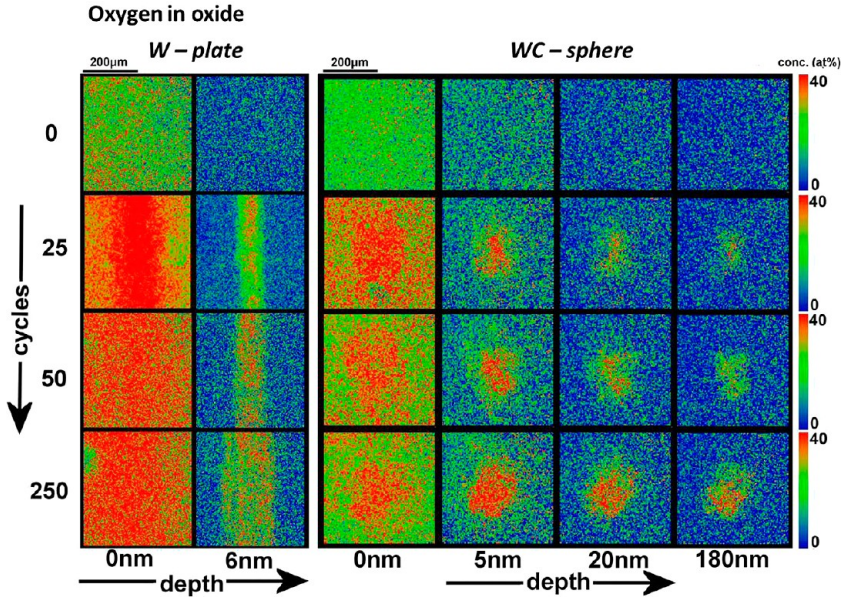

Figure 3. Atomic concentration maps (atom %) of oxygen in metal oxide compound. The size of each image is 400 μm × 400 μm and shows the atomic concentration in a color scale ranging from blue (0 atom %) to green (20 atom %) to red (40 atom %). Left two columns, wear track on tungsten platen; right four columns, tungsten carbide ball contact area.

increasing number of cycles and correspondingly the width of the wear track. Figure 4 shows the distribution of carbon concentration bound as carbide. No transfer from the tungsten carbide counterface onto the tungsten is observed in the region of the wear track. In contrast, the reduced carbide concentration in the center of the tungsten carbide specimen indicates a transfer from the tungsten specimen.

Figure 5 shows the XPS concentration maps of metallic tungsten. Metallic tungsten cannot be directly measured due to the overlap of W 4f photoelectron lines of metallic tungsten and tungsten carbide. Thus, the concentration maps shown in Figure 5 are obtained by subtracting the carbon carbide map from the W 4f map. Nearly equal concentrations of metallic tungsten are found within the contact area of the wear track on the tungsten and that of the tungsten carbide counterface, supporting the assumption that tungsten transfers onto WC. The relatively high metallic tungsten concentrations (~30 atom %) in the center of the tungsten carbide indicate that a considerable amount of nonoxidized metallic tungsten adhered to the tungsten carbide forming the tungsten transferfilm.

Figure 6 shows an example of the TEM analysis of debris particles generated during the wear test. The corresponding diffraction patterns in this figure reveal

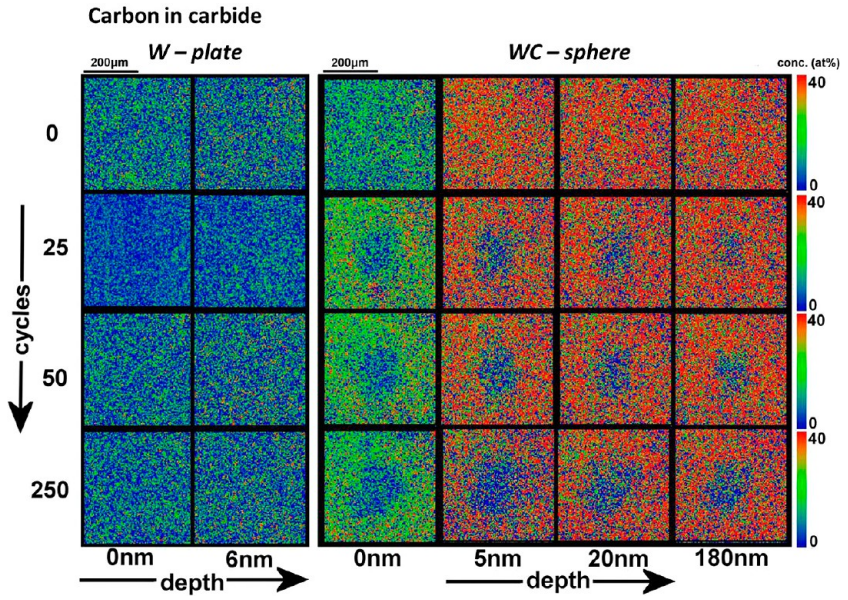

Figure 4. Atomic concentration maps (atom %) of carbon in a tungsten carbide compound. The size of each image is 400 μm × 400 μm and shows the atomic concentration in a three color scale ranging from blue (0 atom %) to green (20 atom %) to red (40 atom %). Left two columns, wear track on tungsten platen; right four columns, tungsten carbide ball contact area.

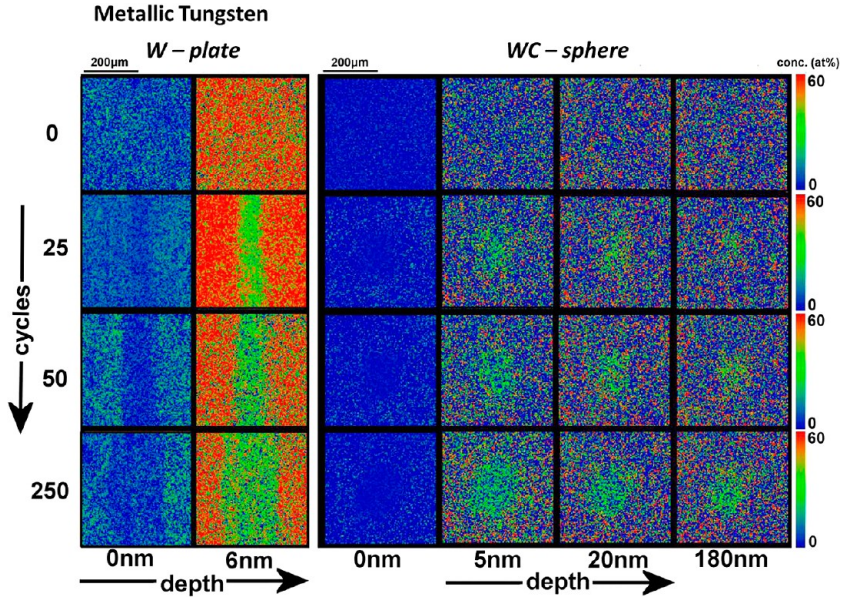

Figure 5. Atomic concentration maps (atom %) of metallic tungsten obtained by subtracting the carbon carbide map from the received W 4f map. The lateral size of each image is 400 μm × 400 μm and shows the atomic concentration in a three color scale ranging from blue (0 atom %) to green (30 atom %) to red (60 atom %). Left two columns, wear track on tungsten platen; right four columns, tungsten carbide ball contact area.

a W_2C particle in the upper frame, while a Co particle is shown in the lower frame. The Co particle shows a high defect density with a polycrystalline structure. In general, the particles have a crystalline structure and are composed of mainly W_2C, WO_2, WO_3, and W. Interestingly, no tungsten carbide in the form of WC is observed within the collected debris particles. The individual crystals of these particles vary in size between 50 and 100 nm indicating a refined grain structure compared to the unworn specimen. The sizes of the debris particles are found to be up to a few micrometers. The individual particle size is usually related to the specific cycle number as well as the wear rates (*i.e.*, large particles correlate to larger wear rates).[16] More specifically, while the wear area increases with the sliding cycles, the wear rate (*i.e.*, depth/sliding distance) is highest within the first few cycles of the test, as shown in earlier work for similar tribocouples.[9] Thus, the larger particles are created during the initial running-in stage, which experiences higher wear rates due to the adaptation/plowing of the two initial rough surfaces. Subsequently, the particles during steady-state are smaller,

which correlates with the lower wear rates and refined grain layer.

Physical Properties of WC/W Third Body. *Evolution of Strength.* The hardness and reduced modulus, obtained from nanoindenation tests, are shown in Figure 7 for the tungsten specimen at three different indentation depths as a function of the number of cycles. Looking at 50 nm indentation depth results, the hardness starts to decrease after the first 10 cycles and reaches values below 10 GPa. During steady state (*i.e.*, 250 cycles), the hardness shows a slight increase but remains within the error of the value at the 50th cycle indicating a constant behavior. Similarly, the reduced modulus decreases initially to values below 100 GPa after about 50 cycles and then remains relatively constant during steady state sliding (*i.e.*at approximately 250 cycles). The same behavior is also observed at higher indentation depth (*i.e.*, 100 and 150 nm). These results, therefore, indicate that there is no significant depth dependence of the hardness and reduced modulus between 50 and 150 nm.

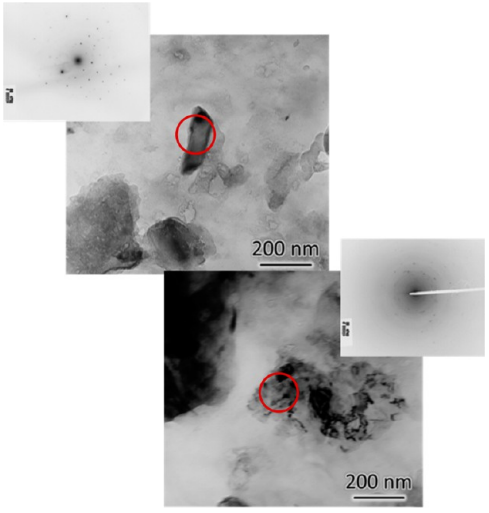

Figure 6. TEM images of debris particles generated during the sliding. The corresponding diffraction patterns reveal that the upper frame shows a W_2C particle, while the lower one shows a Co particle.

Figure 8 shows the nanoindentation results for the tungsten carbide face. The hardness and reduced modulus drastically decrease within the first 25 cycles to values below 5 and 100 GPa, respectively. The hardness and reduced modulus increase slightly after 25 cycles and remain nearly constant during steady state (*i.e.*, 250 cycles). Nanoindentations are also performed outside of the contact area, where mostly debris particles created during sliding are found. The hardness and reduced modulus of these particles show an average value of 1.6 ± 0.2 GPa and 35.4 ± 14.5 GPa, respectively, for indentation depth between 80 and 175 nm, which is lower compared to the mechanically mixed layer within the contact area. While these values provide a rough idea of the properties of the debris particles, it should be

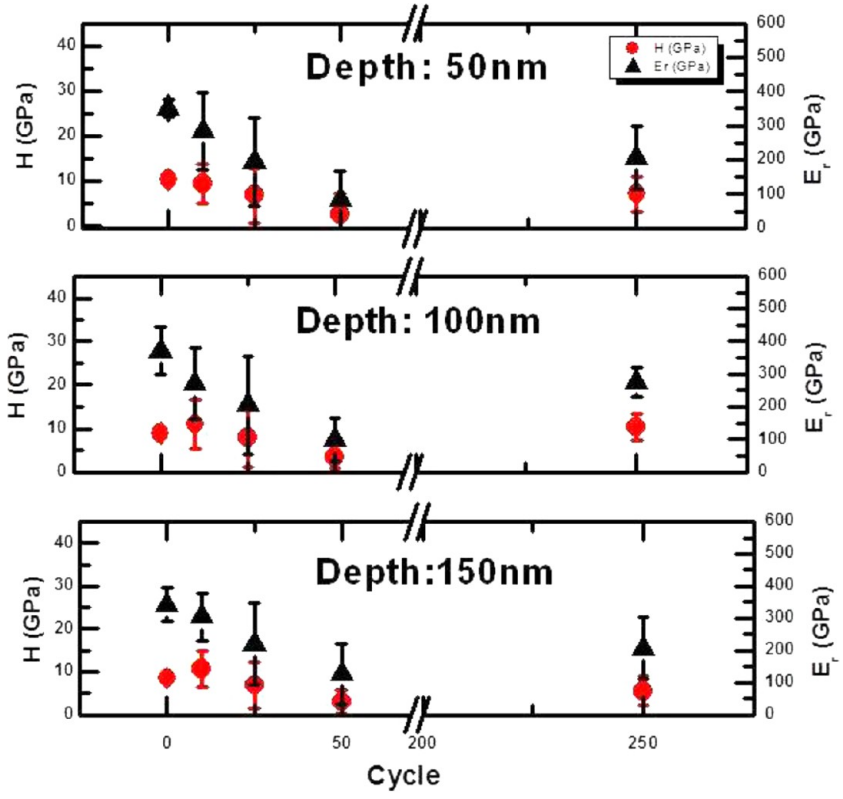

Figure 7. Nanomechanical properties (*i.e.*, *H* and E_r) of the W wear track measured at 50, 100, and 150 nm indentation depths. The hardness is represented with the red spheres, while the reduced modulus is shown with the black triangles. The results indicate that there is no significant depth dependence of the hardness and reduced modulus between 50 and 150 nm.

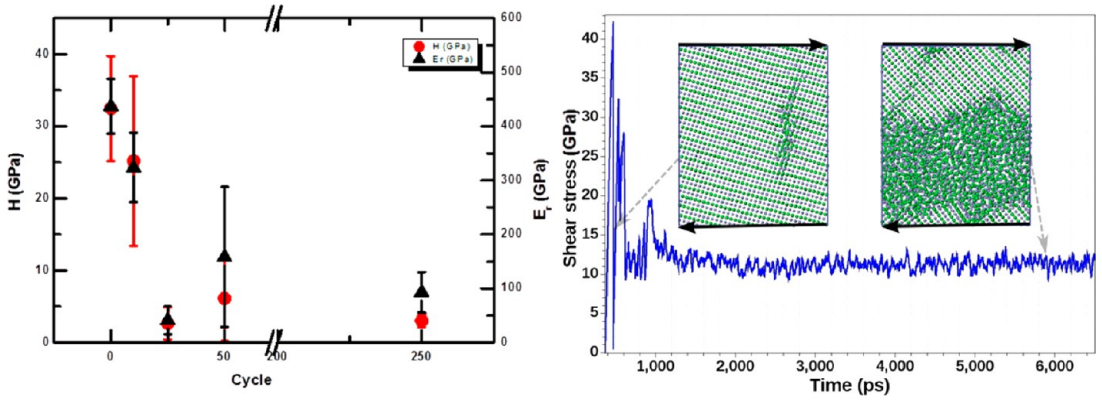

Figure 8. (Left) Experimental measurements of H and E_r of the WC counterface measured between 100 and 200 nm indentation depths and (right) evolution of the shear stress obtained from MD uniform shear simulations (10 m/s shear velocity). The complete simulation with additional analysis is found elsewhere[9]

noted that the actual values of the individual particles might vary due to the different composition, their surface not being flat, as well as uncertainties of the exact contact between the debris and the surface.

As a comparison to the evolution of mechanical strength of W−C third body layers with increasing shearing time (*i.e.*, increasing number of sliding cycles), displayed in Figure 8 (left), Figure 8 (right) presents the evolution of shear resistance exhibited by an initially crystalline WC specimen as predicted by uniform shear MD simulations using Lees Edwards boundary conditions.[17] This atomistic simulation represents the initial stage of sliding underneath an asperity of the WC counterface (*i.e.*, excluding the Co binder), which experimentally consists of mainly WC phases with nearly no W_2C or W_3C phases. The aim of this simulation is to demonstrate how as in the experiments, the tungsten carbide grains exhibit decreasing resistance as their crystalline structure is amorphized. As can be observed, initially, the shear strength is above 40 GPa after which it drops significantly to approximately 10 GPa at ∼500 ps (*i.e.*, 88% shear strain). Subsequently, the shear strength nearly doubles at 1000 ps (*i.e.*, ∼176% shear strain) and then drops to 12 GPa where it remains nearly constant for the remainder of the simulation. The two snapshots in Figure 8 (right) show the atomic structure at the onset of shearing and during saturation of the shear resistance, respectively. The images show that when the shear strength is high, the WC specimen has a crystalline structure, but when the shear stress is low and steady, the WC specimen has a considerably large amorphous region where the shear is accommodated. Comparing the shear stress of the initial state to the stress during steady state shearing, there is a 75% decrease, which is similar to the decrease in hardness values shown in Figure 8 (left).

In addition to nanoindentation experiments, compression tests are performed on a worn tungsten surface to better understand the variation in mechanical properties of the tribo-induced layer. Figure 9 shows typical results in terms of stress *vs* strain for micropillars cut-out of the worn and unworn material after 250 cycles. The plots in Figure 9 indicate that the pillars (*i.e.*, not coated with Pt) cut-out of the worn surface (*i.e.*, mechanically mixed layer) are less resistant to compressive stress compared to the ones extracted from the unworn surface. In addition, the slope of the initial displacement (*i.e.*, considering the linear section without the initial deviations) for the wear track pillars is lower compared to the one of the unworn surface, indicating lower modulus. Therefore, micropillar compression tests, verify the results of the nanoindentaiton tests, namely that the mechanically mixed layer is weaker relative to the unworn surface.

While these results seem promising at first, care must be taken when interpreting micropillar compression tests. To capture the roughness effects on the micropillar compression tests, since the worn surface is rougher compared to the unworn, we also test pillars coated with Pt. These results show similar maximum stresses to the ones of the uncoated pillars within the wear track indicating that roughness has minimal influence on the contact between the flat punch and the pillar. Nevertheless, contact misalignment between the flat punch and the top surface of the pillar should not be completely ruled out.

Quantitative Imaging by Atomic Force Microscopy. Maps of the local adhesion of the worn and unworn surfaces are recorded using atomic force microscopy. The images and histogram for the tungsten surface is shown in Figure 10 for various cycle numbers as well as for the unworn surfaces. Considering the average pull-off force, it is observed that the surface adhesion has drastically decreased after sliding for 10 cycles. The grooves (*i.e.*, valleys) parallel to the sliding are visible in the image after 10 cycles due to the contrasts variations in the pull-off forces; lower pull-off forces are observed within the valleys compared to the edges. This is likely a topography artifact; the contact area between tip and surface is larger at the edges, and thus, the adhesion is higher. After the 10th cycle, the surface adhesion continues to decrease up to cycle 50. During steady state sliding (*i.e.*, cycle 250), the average

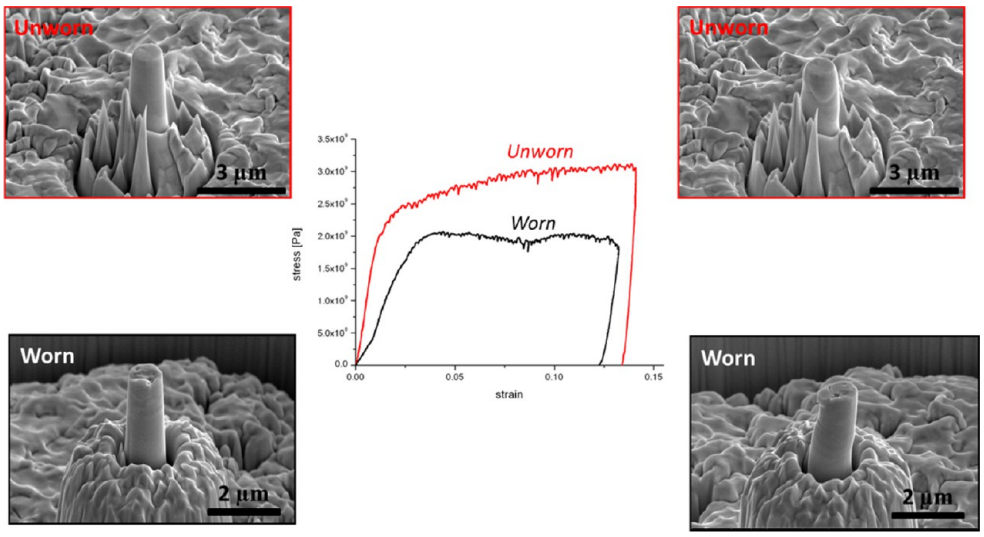

Figure 9. Stress *vs* strain curves obtained from micropillar compression testing of the W wear track and unworn surface. SEM images of the pillars are shown before and after compression.

pull-off force is slightly higher compared to the ones after cycles 25 and 50. A similar behavior is observed in the pull-off force maps and histogram of the counter face, as shown in Figure 10, where the surface adhesion is decreased after 10 cycles. However, it should be noted that during steady state the surface adhesion is lower for the counterface compared to one of the tungsten surface.

Nanoindentation Atomistic Simulations of the W:C Surface. The atomistic nanoindentation models used to investigate the strength of crystalline and amorphous W−C material on the tungsten carbide countersurface are shown in Figure 11. It should be noted that we do not claim to be modeling the experiments exactly. The influence of oxygen is only investigated in the experimental part, where a detailed elemental analysis is performed and correlated to the mechanical properties. Keeping in mind that underneath the surface contaminants shown in the experimental sections, the WC countersurface is composed almost entirely of crystalline WC and as sliding progresses, the surface is mainly composed of amorphous W:C, these material models can be used to probe the strength of the tungsten carbide countersurface before and after sliding in vacuum conditions (*e.g.*, absence of oxygen). For this aspect, the atomistic simulation can provide essential insights into the experimentally observed results.

The crystalline specimen in Figure 11a has a density of 16 240 kg/m^3 and was built by reproducing a WC (*Strukturbericht Bh*) hexagonal unit cell. The amorphous specimen in Figure 11b has a density of 13 620 kg/m^3 and was generated by taking a representative volume of the amorphous phase generated by uniformly shearing an initially crystalline WC specimen. This representative volume of the amorphous phase generated by sliding shear is periodically repeated, relaxed and equilibrated to generate the specimen in Figure 11b.

The resulting indenting/retracting force on the indenter is presented in Figure 12a. It is evident that the contact stiffness is higher for the crystalline WC surface (*i.e.*, unworn) compared to the amorphous (*i.e.*, worn) surface. Thus, the crystalline substrate has a significantly higher resistance to deformation compared to the amorphous sample. For instance at a 20 Å indentation depth, the mean resistance of the crystalline specimen is more than double relative to the amorphous sample. The slope of the unloading curve, which is related to the specimen modulus, is higher for the crystalline sample compared to the amorphous sample. These differences in the resistance between the two substrates (*i.e.*, amorphous and crystalline) can be explained by the differences in the bonding states. With the use of a 2.3 Å cutoff, which captures both W−C and C−C bonds, Figure 12b demonstrates that almost all the atoms in the crystalline specimen are 6-coordianted, while most of the atoms in the amorphous specimen have a coordination of 4 or less. The 2.3 Å cutoff captured only W−C bonds in the crystalline case with all atoms not on a surface having 6 W−C bonds. The same cutoff indicates that atoms in the amorphous system contain predominantly W−C bonds with only ∼7.8% of the C atoms having C−C bonds and only ∼0.5% of the C atoms having C−C bond lengths below 1.85 Å. The lower coordination of the W and C atoms in the amorphous system verifies that a majority of the atoms in the amorphous case are not fully bonded and that a lower density of W−C bonds exists. Furthermore, based on the radial distribution function with a 3.2 Å cutoff that captures both C and W nearest neighbors, Figure 12c indicates that most of the W−C bond lengths in the amorphous substrate are either shorter or longer than the 2.2 Å W−C bond length in the crystalline substrate. Similarly, Figure 12c shows that while the W−W bond

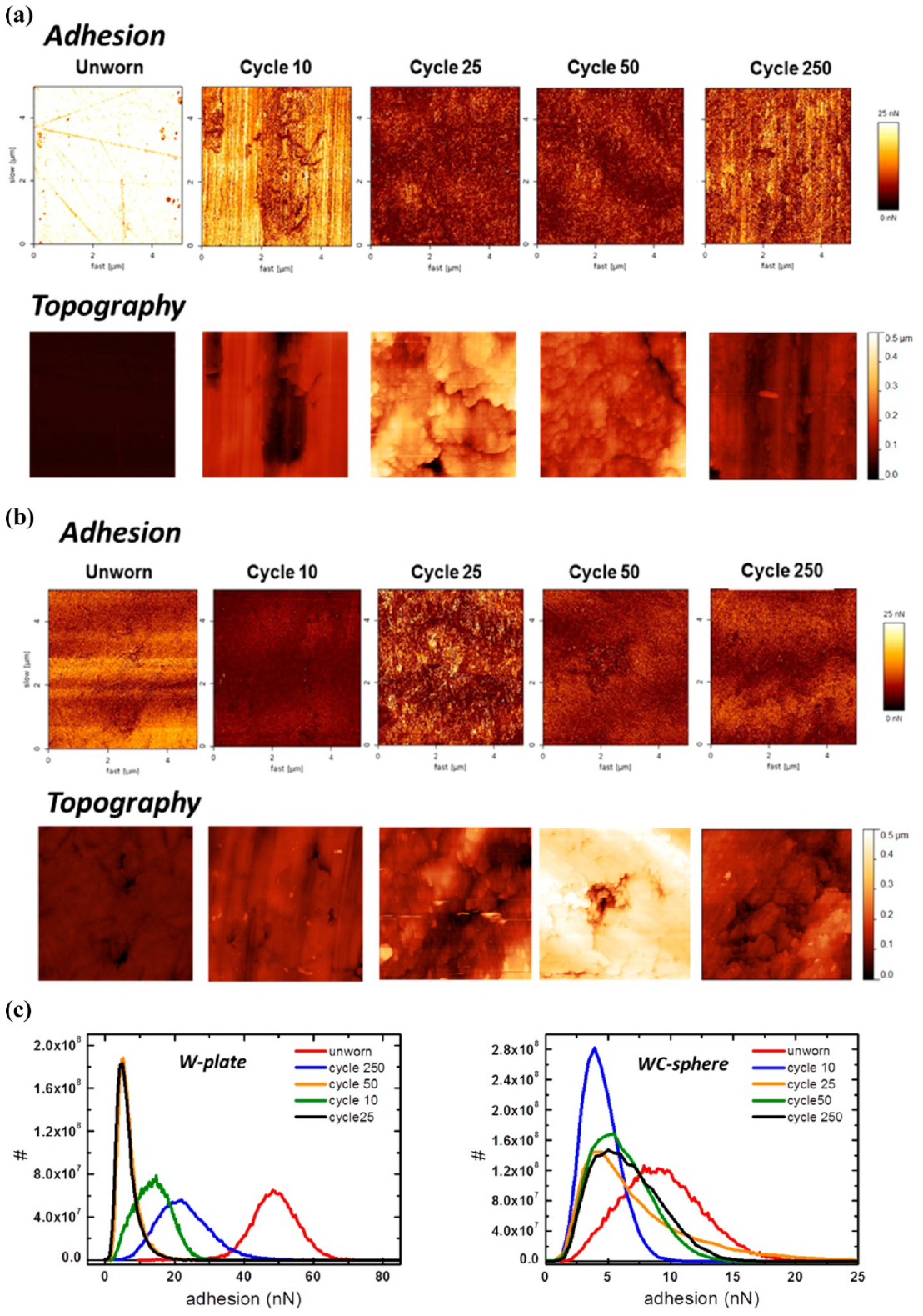

Figure 10. Maps of the AFM pull-off force and the corresponding surface topography of (a) the W wear track, (b) the WC counter face for the unworn and worn surfaces, and (c) the corresponding histogram.

length of 2.91 Å is clear for the crystalline system, this bond length is compressed or stretched for the amorphous system. The lower atom coordination combined with nonequilibrium bonds (*i.e.*, longer or shorter bonds) results in a weaker material microstructure in the amorphous specimen which in turn decreases the specimen's strength as shown in Figure 12a.

Snapshot accompanied by the evolution of the loading and unloading indentation force as a function

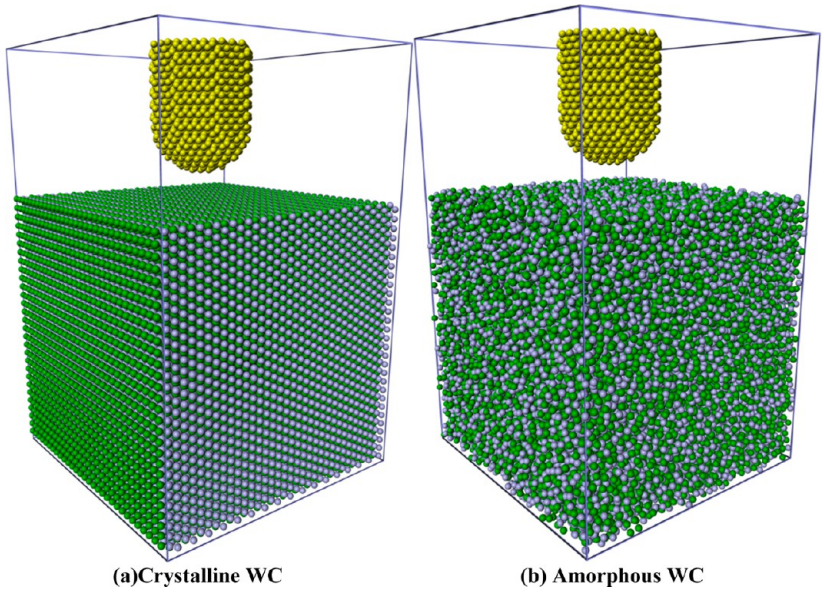

Figure 11. Constructed atomistic nanoindentation models consisting of a rigid/adhesive diamond indenter and (a) a crystalline WC substrate that represents the unworn WC surface material and (b) an amorphous WC substrate that represents the worn W:C surface material. The tungsten atoms are presented in green, the carbon atoms in the WC specimen are light purple, and the carbon atoms in the rigid diamond indenter are yellow.

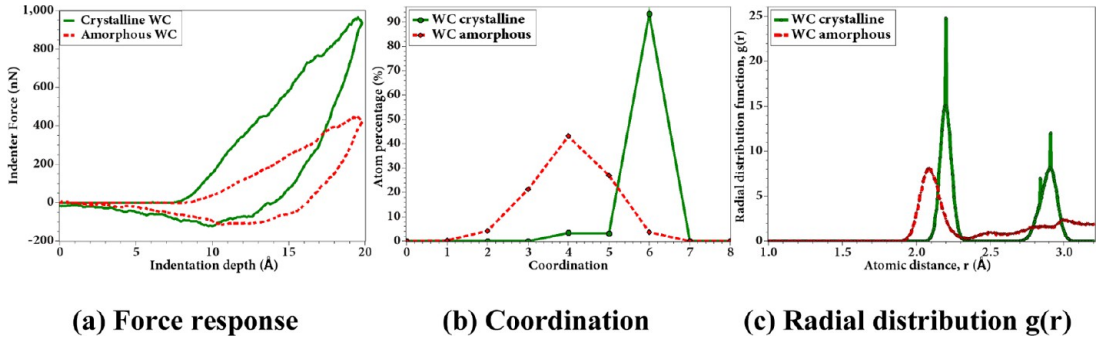

Figure 12. (a) Force *vs* indentation depth obtained from nanoindentation simulations into a crystalline and an amorphous W:C specimen representing the unworn and unworn (*i.e.*, mechanically mixed layer) W:C surface, respectively. (b) The coordination of the crystalline and amorphous W:C specimens (*i.e.*, excluding the rigid diamond indenter) based on a 2.3 Å cutoff, which captures both W−C and C−C bonds within the different specimens. (c) Radial distribution function with a 3.2 Å cutoff that captures both C and W nearest neighbors.

of time are presented in Figure 13 for both the crystalline and the amorphous specimen. Both materials exhibit similar pull-off forces (*i.e.*, ∼125 nN). This occurs because the crystalline substrate is amorphized locally during indentation, and during retraction, the indenter is essentially being retracted from an amorphous region in both cases, as illustrated with the snapshots in Figure 13. These pull-off forces are significantly higher relative to the ones measured in the experiments due to adhesion of the diamond indenter to the WC surfaces *via* C−W and C−C bonds. This adhesion is evident in the snapshots shown in Figure 13, where carbon and tungsten transfer is apparent. The steps in the loading curve (indicated by gray arrows in Figure 13) mark instances of force release due to breaking and amorphization of the WC crystalline surface during indentation. As shown in the snapshots of Figure 13, the rigid diamond indenter deforms the near surface region of the crystalline specimen into an amorphous phase. The generated amorphous phase is still present after retraction of the indenter, which indicates that the W−C amorphous phase is stable at room temperature (*i.e.*, 300 K). Similar behavior has been previously observed in nanoindentation atomistic simulations of various crystalline solids.[18−20] The remaining atoms within the contact area of the crystalline sample form a small pile-up on the surface, while significantly less pile-up is observed on the amorphous sample, which could be explained by the amorphization requiring more space. Such pile-up has been previously observed in MD simulations of nanoindentations on Fe_xC.[21]

DISCUSSION

The sliding of tungsten carbide against tungsten results in third body formation consisting of grain

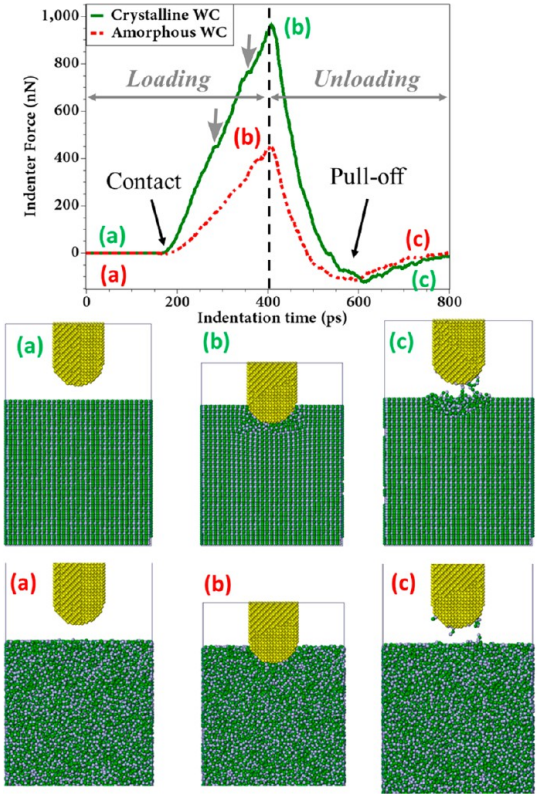

Figure 13. Indenter force *vs* indentation time obtained from nanoindentation simulations for an amorphous and a crystalline specimen representing the mechanically mixed layer and unworn surface, respectively. Snapshots (a) to (c) along the force evolution plot show the progression from indentation to retraction.

refinement of the W surface and a mechanically mixed amorphous layer on the WC counterface. To elucidate the influence of the structural changes on the friction and wear response of a system, it is important to discuss the evolution of their surface strength (*i.e.*, hardness, reduced modulus, and resistance to microcompression) in comparison with their chemical state. The experimental results obtained by nanoindentation show decreased hardness and reduced moduli of the mechanically mixed layer on the tungsten carbide counter face compared to the unworn surface. Similarly, the wear track on the pure tungsten sample reveals lower reduced modulus compared to the unworn surface. However, the hardness of the worn tungsten surface does not show a significant difference compared to the unworn state.

The mechanically mixed layer of the tungsten carbide counter face is softer (*i.e.*, lower hardness and reduced modulus values) compared to the one of the worn tungsten. Consequently, the percent decrease in hardness and reduced modulus of the tungsten carbide tribolayer is higher compared to the one of the tungsten during steady state. This behavior correlates well with the shear strength values obtained from simulations of such materials using Lees Edwards boundary condition in a previous study;[9] while the shear stress of the tungsten specimen did not change significantly after shearing, the shear stress of the WC sample decreases by approximately 75% after 3000 ps compared to the initial state. These variations in the evolution of the shear stresses can be explained by differences in the shearing accommodation modes. Shearing of the tungsten specimen results in nucleation of dislocations, while the tungsten carbide forms an amorphous phase upon shearing. The different phase transformations caused by shearing have also been observed experimentally in a previous study,[9,10] elucidating the variations in the evolution of the mechanical properties between the two surfaces (*i.e.*, WC and W). It is remarkable, however, that no nucleation of dislocations is observed within the tungsten carbide specimen upon shearing, which deviated from our understanding of the deformation mechanism in tungsten carbides.[22,23]

To gain further insights on the softening (*i.e.*, decrease in hardness and reduced modulus) of the mechanically mixed layer on the WC counter face, we performed nanoindentation molecular dynamics simulations. On the basis of the evolution of the substrate stress during the simulations, the crystalline tungsten carbide specimen exhibited higher strength relative to the amorphous phase. These observations are consistent with previous models on predicting the hardness of solids,[24−26] which indicate that the hardness is directly related to the chemical bonds in terms of their combined resistance to the indenter, as reviewed by Tian *et al.*[24] Similarly, Simunek *et al.*[26] predicted that the hardness is directly proportional to the bond strength within the system, which correlates well with the observations from the atomistic simulations in our study. As indicated by several hardness prediction models,[27] besides the average bond strength, the hardness in a solid has a strong dependence on the number of bonds per unit volume, the number of valence electrons per atom, and the amount of covalent bonds.

While the atomistic simulations provide important insights on the underlying mechanisms of the WC deformation, it is not a direct representative of the experiments due to the lack of oxygen. Thus, we perform some detailed chemical and structural analysis of the worn surfaces using XPS and TEM in order to capture the effects of the oxygen on the structure and mechanical properties. The XPS analysis (*i.e.*, mapping and depth profiling) reveals an increase in the oxygen concentration of both surfaces, mostly in the WO_2 state. Increased oxide concentrations in tungsten have previously been shown to soften tungsten[28−30] or tungsten carbide.[31] Polcar *et al.*[29] saw a decrease in hardness from 25 (*i.e.*, 13 atom % O) down to 7.7 GPa (*i.e.*, 75 atom % O) for tungsten oxide films, which they explained by the amorphization of the coating associated with the increase of the W−O ionic bond in the higher oxide content coating. This behavior can further

explain the decrease in strength of the tungsten carbide tribofilm compared to the unworn state in our study. Interestingly, while the oxide content is also higher in the near surface region of the tungsten wear track, the decrease in strength compared to the unworn state is not as apparent. This observation seems contradictory to the chemical analysis and previous literature on tungsten oxides. However, considering the grain-refinement in the near surface region of the tungsten wear track during steady state sliding, it becomes evident that this effect is due to the size-dependent mechanical behavior (*i.e.*, Hall Patch effect),[32,33] which correlates the mechanical strength to the average grain size. In this particular case, the grain refined layer in the near surface region of the tungsten specimen, induced by the sliding, causes an increase in hardness, while the tungsten oxide concentration decreases it, resulting in similar strength to the unworn state.

In comparison to the experimental and simulated nanoindentations, the micropillar compression tests revealed a similar behavior, showing a higher resistance to the compression for the unworn surface. This is somewhat surprising since it does not agree with literature on the strength of tribofilms in single crystal nickel,[13] where the results from the nanoindentations deviate from the pillar compression tests; nanoindentations indicated that the worn surface is harder compared to the unworn, while pillar compression showed the opposite. The authors explained this contradiction by the pre-existing dislocations in the pillars of the worn surface, causing them to be softer. However, the material in their study is Nickel, which has a face centered cubic (FCC) crystal structure, while in our study the tungsten's is body centered cubic (BCC). Schneider *et al.*[34] showed that prestraining does not systematically influence the yield strength of BCC materials and has a negligible effect on stress−strain behavior of the pillars, suggesting that dislocation storage does not occur in small-scale BCC specimens. In addition, while the prestraining effect mentioned by Battaile *et al.*[13] might still be the case for the worn tungsten pillars in our study, the increased oxide content (*e.g.*, WO_2 state) in the worn surface is probably more significant in decreasing the strength of the pillars.

Besides having a major effect on the mechanical properties, the increased oxide concentration in the near surface region caused by the sliding showed to have also an influence on the surface adhesion. Adhesion imaging of the worn tungsten and tungsten carbide surfaces shows lower pull-off forces compared to the unworn state. The atomistic simulations, on the other hand show similar pull-off forces for the worn and unworn state; upon retraction of the diamond tip, the carbon (*i.e.*, from the W:C surface) bonds to the tip increasing the pull-off forces. This difference in the surface adhesion between the simulations and experiments can be explained by the high oxide concentration on the surface, as observed with the XPS analysis. It is likely that the oxide concentration causes passivation of the surface resulting in lower surface energy and thus lower surface adhesion compared to pure tungsten or tungsten carbide.

CONCLUSION

This study investigated the properties of the tribolayer generated between ceramic/metal sliding couples (*i.e.*, WC/W) in terms of their deformation mechanisms, nanomechanical properties (*i.e.*, hardness and reduced modulus), surface adhesion, and chemical composition. The experimental results from the nanoindentations and micropillar compression testing indicate a decrease in mechanical properties as a function of the cycle number. The chemical analysis further suggests that the decrease in hardness and reduced modulus of the amorphous layer is attributed to the increased oxide concentration in the mechanically mixed layer as well as metallic (*i.e.*, tungsten) transfer onto the counterface. Additionally, the higher oxide content causes a decrease in surface adhesion, as observed by means of quantitative adhesion mapping, resulting in steady state sliding. Uniform shear and nanoindentation molecular dynamics simulations are then conducted in order to probe the strength of the WC surface at the atomic level, which helps explain/verify certain aspects of the experimental findings. These simulations indicate that this difference in the resistance between the two substrates (*i.e.*, amorphous and crystalline representing the worn and unworn specimen) is explained by the differences in the bonding state; the atoms in the amorphous state have a lower coordination number with a higher number of nonequilibrium bonds compared to the crystalline specimen contributing to the decrease in the indentation modulus. These observations correlate well with the properties obtained from the nanoindentations and micropillar compression experiments.

METHODS

Macroscale sliding experiments are performed using an "online" tribometer. The instrumentation is described in detail elsewhere.[35] It is equipped with a force sensor, a holographic microscope and an atomic force microscope allowing for monitoring topographical changes after each cycle. The experiments are performed on a 99.9 wt % tungsten plate obtained from Goodfellow GmbH in the "as rolled" condition and polished down to a RMS roughness of 34 ± 4 nm. Cross-sectional SEM images obtained from Focused Ion Beam (FIB) cuts of the sample prior to the sliding experiments reveal that the polishing procedure does not have a significant influence on the near surface structure.[9] Similarly, XPS analysis of the unworn surface shows no significant changes in the chemical composition

(*e.g.*, oxide layers) after the polishing procedure.[9] WC–Co spheres (94% WC and 6% Co–obtained from Spherotech GmbH) with a radius of 1.5 mm are used as counter face for the sliding tests. The experiments are performed with a sliding velocity of 5 mm/s and an initial normal load of 2 N in reciprocating mode. Sliding experiments are performed for various cycle numbers in order to observe the evolution of the interfacial processes.

Ex situ chemical analysis of the worn surfaces (*i.e.*, plates and counter faces) is performed using X-ray photoelectron spectroscopy (XPS) (Axis Nova, Kratos Analytical) and TEM (EM 400, by Philips). The different binding states observed in XPS are distinguished by the chemical shift of the electron binding energy of the prominent photoelectron lines. In the case of carbon, oxygen and tungsten these are C 1s, O 1s and W 4f. Concentration depth profiles are obtained by iterative removal of surface layers by ion etching (2 keV Ar^+) and continuous XPS analysis. Lateral elemental concentration distributions are also obtained by parallel imaging XPS spectroscopy. In conjunction with sputtering, three-dimensional chemical information on the near-surface region is obtained in the form of tomographic slices, each one being an elemental concentration map in a certain sputter depth. The XPS results are compared to the analysis performed on the unworn surface using the same methodology. The wear depth and third body thickness are measured from images obtained with a white-light interferometer (WLI) (Wyko NT3300 Optical 3D Profiling System). In addition, quantitative imaging of the worn and unworn surfaces is performed using an atomic force microscope (JPK Instruments, NanoWizard3) with a set point of 150 nN and a Z length of 80 nm. A Nanosensors PPP-NCLR cantilever is used with a spring constant of 35.51 N/m. The scan size is $5 \times 5\ \mu m^2$ with 256×256 pixels. The same cantilever is used for all experiments, however, the imaging is performed in randomized order with respect to cycle number in order to account for any changes in the contact area.

Nanoindentation and micropillar compression techniques are applied in order to study the strength of the deformed surfaces. A Hysitron TriboIndenter 950 system with a diamond Berkovich tip ($R \sim 150$ nm) is used for the nanoindentations and the maximum indentation depth is varied between 50 and 150 nm. A total of 180 indentations are performed on the tungsten wear tracks (*i.e.*, 50, 100, and 150 nm indentation depth at sliding cycles of 0, 10, 25, 50, and 250 cycles). The total amount of indentations carried out on the WC spheres is 160 (*i.e.*, 20 on an unworn tungsten carbide sphere and 140 on the worn spheres for the various cycle numbers). The same instrumentation with a diamond flat punch of 10 μm in diameter is also used for the micropillar-compression experiments. The pillars, with a radius of 1 μm and aspect ratio (length:diameter) of 3:1, are developed using a Focused Ion Beam (FIB) (Versa 3D DualBeam, FEI) equipped with a gallium ion source. The FIB milling procedure is performed in two steps as shown by Volkert and Lilleodden.[36] A beam voltage of 30 kV and beam currents ranging between 1 nA and 30 pA are used. The last steps are carried out at very low currents in order to reduce the gallium ion damage of the pillars and adjust the final size of the pillars. It must be noted that, with such pillar milling approach, pillars with the shape of a truncated cone are produced. The measured tapering angle of all pillars was $2.1° \pm 0.6°$. For this study, we test a total of eight pillars; two are coated with Pt. Pillars coated with Pt are compared to uncoated pillars in order to see the influence of surface roughness. The pillars are compressed in displacement control at a displacement rate of 5 nm/s and up to a strain of 15%.

Classical molecular dynamics simulations of simple uniform shear and nanoindentation were performed with the intent of providing atomistic insights into the experimentally observed properties of the W–C third body material. We note that the aim of the simulations is not to exactly reproduce the experiments but rather to atomistically probe the mechanical strength of crystalline and amorphous WC materials. Despite differences in indentation velocity, system size and environmental conditions between the two methods (*i.e.*, experiments and simulations), the performed atomistic simulations are capable of providing essential insights into the experimentally observed material properties.[37–44] The simulations were performed using a screened version[9] of the bond-order potential for tungsten–carbon-hydrogen systems developed by Juslin *et al.*[45] The shear simulations were carried out by subjecting a pristine monocrystalline WC specimen (size: 46.5 by 25.2 by 56.7 Å) to simple uniform shear at 10 m/s ($1.851\ ns^{-1}$) using Lees Edwards boundary conditions.[17] The specimen was thermostated at 300 K using Langevin dynamics[46] while being sheared. The nanoindentation simulations were performed using an adhesive rigid spherical (radius = 10 Å) diamond indenter and either a crystalline or an amorphous WC rectangular substrate, representing an unworn and a worn tungsten carbide subsurface, respectively. The dimensions of the amorphous WC substrate were $84.91 \times 82.59 \times 84.20$ Å, while the dimensions of the crystalline WC substrate were $83.69 \times 83.90 \times 82.82$ Å with the (1010) surface being indented.

Conflict of Interest: The authors declare no competing financial interest.

Acknowledgment. We thank the Deutsche Forschungsgemeinschaft for financial support under contracts FI451, MO879, SCH425 and KO 120/12-1 as well as CRC 926 (MICOS) and DI1494. The authors would also like to thank Alfons Fischer for helpful discussions. Finally, we gratefully acknowledge the computing time granted under project No. hfr09 on the supercomputer JUROPA at NIC Jülich Supercomputing Centre.

REFERENCES AND NOTES

1. Rigney, D. A. Transfer, Mixing and Associated Chemical and Mechanical Processes during the Sliding of Ductile Materials. *Wear* **2000**, *245*, 1–9.
2. Rigney, D.; Karthikeyan, S. The Evolution of Tribomaterial During Sliding: A Brief Introduction. *Tribol. Lett.* **2010**, *39*, 3–7.
3. Sriraman, K. R.; Strauss, H. W.; Brahimi, S.; Chromik, R. R.; Szpunar, J. A.; Osborne, J. H.; Yue, S. Tribological Behavior of Electrodeposited Zn, Zn–Ni, Cd and Cd–Ti Coatings on Low Carbon Steel Substrates. *Tribol. Int.* **2012**, *56*, 107–120.
4. Wang, X. J.; Rigney, D. A. Sliding Behavior of Pb-Sn Alloys. *Wear* **1995**, *181–183* (Part 1), 290–301.
5. Godet, M. The Third-body Approach: A Mechanical View of Wear. *Wear* **1984**, *100*, 437–452.
6. Sawyer, W. G.; Wahl, K. J. Accessing Inaccessible Interfaces: *In Situ* Approaches to Materials Tribology. *MRS Bull.* **2008**, *33*, 1145–1150.
7. Wahl, K. J. Macroscale to Microscale Tribology. *Micro- and Nanoscale Phenomena in Tribology*; CRC Press: Boca Raton, FL, 2011; pp 5–22.
8. Wahl, K. J.; Sawyer, W. G. Observing Interfacial Sliding Processes in Solid–Solid Contacts. *MRS Bull.* **2008**, *33*, 1159–1167.
9. Stoyanov, P.; Romero, P. A.; Järvi, T. T.; Pastewka, L.; Scherge, M.; Stemmer, P.; Fischer, A.; Dienwiebel, M.; Moseler, M. Experimental and Numerical Atomistic Investigation of the Third Body Formation Process in Dry Tungsten/Tungsten-carbide Tribo Couples. *Tribol. Lett.* **2013**, *50*, 67–80.
10. Stoyanov, P.; Stemmer, P.; Järvi, T.; Merz, R.; Romero, P.; Scherge, M.; Kopnarski, M.; Moseler, M.; Fischer, A.; Dienwiebel, M. Friction and Wear Mechanisms of Tungsten-carbon Systems: A Comparison of Dry and Lubricated Conditions. *ACS Appl. Mater. Interfaces* **2013**, *5* (13), 6123–6135.
11. Stoyanov, P.; Romero, P. A.; Merz, R.; Kopnarski, M.; Stricker, M.; Stemmer, P.; Dienwiebel, M.; Moseler, M. Nanoscale Sliding Friction Phenomena at the Interface of Diamond-like Carbon and Tungsten. *Acta Mater.* **2014**, *67*, 395–408.
12. Shakhvorostov, D.; Pinto, H.; Pyzalla, A.; Enders, S.; Pöhlmann, K.; Scherge, M. Mechanical Properties of Tribologically Modified Nano-layers. *Tribotest* **2004**, *11*, 95–102.
13. Battaile, C. C.; Boyce, B. L.; Weinberger, C. R.; Prasad, S. V.; Michael, J. R.; Clark, B. G. The Hardness and Strength of Metal Tribofilms: An Apparent Contradiction between

Nanoindentation and Pillar Compression. *Acta Mater.* **2012**, *60*, 1712–1720.
14. Rupert, T. J.; Schuh, C. A. Sliding Wear of Nanocrystalline Ni–W: Structural Evolution and the Apparent Breakdown of Archard Scaling. *Acta Mater.* **2010**, *58*, 4137–4148.
15. Meshi, L.; Samuha, S.; Cohen, S. R.; Laikhtman, A.; Moshkovich, A.; Perfilyev, V.; Lapsker, I.; Rapoport, L. Dislocation Structure and Hardness of Surface Layers under Friction of Copper in Different Lubricant Conditions. *Acta Mater.* **2011**, *59*, 342–348.
16. Hanke, S.; Samerski, I.; Schöfer, J.; Fischer, A. The Role of Wear Particles under Multidirectional Sliding Wear. *Wear* **2009**, *267*, 1319–1324.
17. Lees, A. W.; Edwards, S. F. The Computer Study of Transport Processes under Extreme Conditions. *J. Phys. C: Solid State Phys.* **1972**, *5*, 1921.
18. Zhao, H.; Zhang, P.; Shi, C.; Liu, C.; Han, L.; Cheng, H.; Ren, L. Molecular Dynamics Simulation of the Crystal Orientation and Temperature Influences in the Hardness on Monocrystalline Silicon. *J. Nanomater.* **2014**, *2014*, 8.
19. Lin, Y.-H.; Jian, S.-R.; Lai, Y.-S.; Yang, P.-F. Molecular Dynamics Simulation of Nanoindentation-induced Mechanical Deformation and Phase Transformation in Monocrystalline Silicon. *Nanoscale Res. Lett.* **2008**, *3*, 71–75.
20. Fang, T.-H.; Chang, W.-Y.; Huang, J.-J. Dynamic Characteristics of Nanoindentation using Atomistic Simulation. *Acta Mater.* **2009**, *57*, 3341–3348.
21. Goel, S.; Joshi, S. S.; Abdelal, G.; Agrawal, A. Molecular Dynamics Simulation of Nanoindentation of Fe_3C and Fe_4C. *Mater. Sci. Eng., A* **2014**, *597*, 331–341.
22. Bolton, J. D.; Redington, M. Plastic Deformation Mechanisms in Tungsten Carbide. *J. Mater. Sci.* **1980**, *15*, 3150–3156.
23. Engqvist, H.; Ederyd, S.; Axén, N.; Hogmark, S. Grooving Wear of Single-crystal Tungsten Carbide. *Wear* **1999**, *230*, 165–174.
24. Tian, Y.; Xu, B.; Zhao, Z. Microscopic Theory of Hardness and Design of Novel Superhard Crystals. *Int. J. Refract. Met. Hard Mater.* **2012**, *33*, 93–106.
25. Gao, F.; He, J.; Wu, E.; Liu, S.; Yu, D.; Li, D.; Zhang, S.; Tian, Y. Hardness of Covalent Crystals. *Phys. Rev. Lett.* **2003**, *91*, 015502.
26. Šimunek, A. How to Estimate Hardness of Crystals on a Pocket Calculator. *Phys. Rev. B* **2007**, *75*, 172108.
27. Sarin, V. K.; Mari, D.; Llanes, L.; Nebel, C. E. *Comprehensive Hard Materials: Hardmetals Ceramics Super Hard Materials*; Elsevier: Waltham, MA, 2014.
28. Polcar, T.; Parreira, N. M. G.; Cavaleiro, A. Tungsten Oxide with Different Oxygen Contents: Sliding Properties. *Vac.* **2007**, *81*, 1426–1429.
29. Polcar, T.; Cavaleiro, A. Structure; Mechanical Properties and Tribology of W–N and W–O Coatings. *Int. J. Refract. Met. Hard Mater.* **2010**, *28*, 15–22.
30. Parreira NJMC, N. M. G.; Cavaleiro, A. Synthesis, Structural and Mechanical Characterization of Sputtered Tungsten Oxide Coatings. *Thin Solid Films* **2006**, *510*, 191–196.
31. Acchar, W.; Gomes, U. U.; Kaysser, W. A. Goring J. Strength Degradation of a Tungsten Carbide-Cobalt Composite at Elevated Temperatures. *Mater. Charact.* **1999**, *43*, 27–32.
32. Jang, J. S. C.; Koch, C. C. The Hall-Petch Relationship in Nanocrystalline Iron Produced by Ball Milling. *Scr. Metall. Mater.* **1990**, *24*, 1599–1604.
33. Meyers, M.; Mishra, A.; Benson, D. The Deformation Physics of Nanocrystalline Metals: Experiments, Analysis, and Computations. *JOM* **2006**, *58*, 41–48.
34. Schneider, A. S.; Clark, B. G.; Frick, C. P.; Gruber, P. A.; Arzt, E. Effect of Pre-Straining on the Size Effect in Molybdenum Pillars. *Philos. Mag. Lett.* **2010**, *90*, 841–849.
35. Korres, S.; Dienwiebel, M. Design and Construction of a Novel Tribometer with Online Topography and Wear Measurement. *Rev. Sci. Instrum.* **2010**, *81* (6), 063904.
36. Volkert, C.; Lilleodden, E. Size effects in the Deformation of Sub-micron Au Columns. *Philos. Mag.* **2006**, 5567–5579.
37. Fang, T.-H.; Wu, J.-H. Molecular Dynamics Simulations on Nanoindentation Mechanisms of Multilayered Films. *Comput. Mater. Sci.* **2008**, *43*, 785–790.
38. Shi, Y.; Falk, M. L. Simulations of Nanoindentation in a Thin Amorphous Metal Film. *Thin Solid Films* **2007**, *515*, 3179–3182.
39. Nair, A. K.; Parker, E.; Gaudreau, P.; Farkas, D.; Kriz, R. D. Size Effects in Indentation Response of Thin Films at the Nanoscale: A Molecular Dynamics Study. *Int. J. Plast.* **2008**, *24*, 2016–2031.
40. Szlufarska, I. Atomistic Simulations of Nanoindentation. *Mater. Today* **2006**, *9*, 42–50.
41. Verkhovtsev, A. V.; Yakubovich, A. V.; Sushko, G. B.; Hanauske, M.; Solov'yov, A. V. Molecular Dynamics Simulations of the Nanoindentation Process of Titanium Crystal. *Comput. Mater. Sci.* **2013**, *76*, 20–26.
42. Saraev, D.; Miller, R. E. Atomic-scale Simulations of Nanoindentation-induced Plasticity in Copper Crystals with Nanometer-sized Nickel Coatings. *Acta Mater.* **2006**, *54*, 33–45.
43. Wang, W.; Li, S.; Min, J.; Yi, C.; Zhan, Y.; Li, M. Nanoindentation Experiments for Single-layer Rectangular Graphene Films: A Molecular Dynamics Study. *Nanoscale Res. Lett.* **2014**, *9*, 41.
44. Lilleodden, E. T.; Zimmerman, J. A.; Foiles, S. M.; Nix, W. D. Atomistic Simulations of Elastic Deformation and Dislocation Nucleation during Nanoindentation. *J. Mech. Phys. Solids* **2003**, *51*, 901–920.
45. Juslin, N.; Erhart, P.; Traskelin, P.; Nord, J.; Henriksson, K. O. E.; Nordlund, K.; Albe, K. Analytical Interatomic Potential for Modeling Nonequilibrium Processes in the W-C-H System. *J. Appl. Phys.* **2005**, *98*, 123520.
46. Schneider, T.; Stoll, E. Molecular-dynamics Study of a Three-dimensional One-component Model for Distortive Phase Transitions. *Phys. Rev. B* **1978**, *17*, 1302–1322.